Engineering Fracture Mechanics 169 (2017) 35–53

Contents lists available at ScienceDirect

Engineering Fracture Mechanics

journal homepage: www.elsevier.com/locate/engfracmech

A J-integral approach in characterizing the mechanics of a horizontal crack embedded in a cantilever beam under an end transverse force

Xiaomin Fang, Panos G. Charalambides *

Department of Mechanical Engineering, University of Maryland, Baltimore County, Baltimore, MD 21250, USA

ARTICLE INFO

Article history:
Received 23 June 2016
Received in revised form 28 October 2016
Accepted 8 November 2016
Available online 11 November 2016

Keywords:
J-integral
Embedded
Horizontal
Crack
Cantilever beam

ABSTRACT

For a cantilever beam with an embedded sharp crack and subjected to an end transverse force, the J-integral approach was employed in developing analytical estimates of the energy release rate made available to the left and right crack tip. Finite element studies also revealed that mode II conditions dominate the tip regions of such a crack (Fang and Charalambides, 2015). Thus, analytical estimates of the mode II stress intensity factor dominating each of the crack tip regions are also obtained. The analytical energy release rate predictions are compared to 2-D finite elements for a broad range of crack depths and crack center location along the beam axis. Using energy considerations, rotary spring stiffness estimates employed in Charalambides and Fang (2016a,b) in the development of a four-beam model obtained. The outcomes of the methodology used in this work provide strong encouragement in extending the method to heterogeneous composite laminates containing delamination cracks and subjected to a combination of applied loadings. Given the predominately mode II nature of the crack considered, the solutions developed herein may be used in characterizing mode II interface fracture for bonded homogeneous layered beams.

1. Introduction

A crack embedded in an elastic, homogeneous and isotropic system is known to propagate in a direction of maximum energy release rate experienced by incipient kink cracks (i.e., cracks of "zero length" compared to the cracked length) at the crack tip [4–7]. For example, under mode I crack surface opening conditions, such an incipient kink crack directly ahead of the crack tip, i.e., residing on the crack plane, experiencing maximum energy release rate and such it is the one activated during crack growth initiation thus confining the macro-crack path to the crack plane as shown schematically in Fig. 1a. However, under pure relative crack surface sliding conditions, i.e., pure mode II loading conditions (see Fig. 1b), local maximum in the energy release rate is experienced by a kink crack at approximately $\theta^k \approx 70.3^\circ$ clockwise from the crack plane for a positive K_{II}, where K_{II} is the mode II stress intensity factor (SIF). In the latter case, a crack embedded in a homogeneous and isotropic medium would kink out-of-plane along the maximum energy release rate kink direction as shown in Fig. 1b. Interestingly, the kink crack path direction predicted using a maximum energy release rate criterion coincides with a path that is perpendicular to the maximum principal stress near the crack tip. Regardless of the criterion used, embedded cracks in homogeneous and isotropic systems would not propagate in their original plane if a mode II component exists. Given the

* Corresponding author.
E-mail address: panos@umbc.edu (P.G. Charalambides).

http://dx.doi.org/10.1016/j.engfracmech.2016.11.010
0013-7944/

Nomenclature

x	coordinate along the beam length
x_C	coordinate of the sharp crack center
y	coordinate along the beam height, or analytical deflection along neutral axis of the slender beam in $x-y$ plane
y_C	coordinate of the sharp crack center
a	half of crack length
l	crack length
L	beam length
l_1	length of sub beam, between the left tip of the horizontal crack to the beam fixed end
l_3	length of sub beam
h	beam height
t	beam width
F	concentrated force
P	load
E	elastic modulus
v	Poisson's ratio
G	shear modulus
N	axial force
V	shear force
M	bending moment
I	cross-sectional second moment of inertia
A	cross-sectional area
Γ	contour
J	J-integral
C	beam compliance
$\Im$	energy release rate
$\Im_c$	characteristic energy release rate
t	subscript or superscript denoting the quantity for the top beam
b	subscript or superscript denoting the quantity for the bottom beam
A	subscript denoting the quantity at Section A
B	subscript denoting the quantity at Section B
C	subscript denoting the quantity at the crack center or at the section passing through the crack center
MM	superscript denoting the quantity derived from analytical four beam model
$COMP$	superscript denoting the quantity derived from compliance method
cr	superscript denoting the crack related quantity
λ	transition region length parameter, dimensionless
σ	stress
ε	strain
δ	deflection
Δ	difference
φ	rotation of beam cross section
ϑ	rotation of beam cross section with shear effects
k	timoshenko shear constant
θ	crack orientation
K_I	mode I stress intensity factor (SIF)
K_{II}	mode II stress intensity factor (SIF)
h_t	distance between the horizontal crack plane and the beam top surface, also known as crack depth
h_b	distance between the horizontal crack plane and the beam bottom surface
Φ	strain energy
w	strain energy density

findings reported elsewhere [1], one would have difficulties to envision the conditions under which mode II crack such as a horizontal crack embedded in a cantilever beam under an end force loading, would initiate and grow in plane as modeled in this study over the lifetime of a component. In all likelihood, cracks developed during the life of a component such as a cantilever beam would most likely initiate and grow in the tensile region normal to the bending stress. Thus, one would expect to see such cracks to be oriented perpendicular to the beam axis, most likely originating from a surface flaw and growing vertically towards the beam neutral axis thus forming a typical edge mode I crack. It is thus not surprising that many crack detection studies [8–12] have indeed been conducted for edge cracks under mode I conditions for which empirical solutions for the stress intensity factor do exist. However, no such rigorous fracture mechanics methods have been used in crack detection studies involving a horizontal, fully embedded crack, perhaps due to their focus on detecting damage in homogeneous

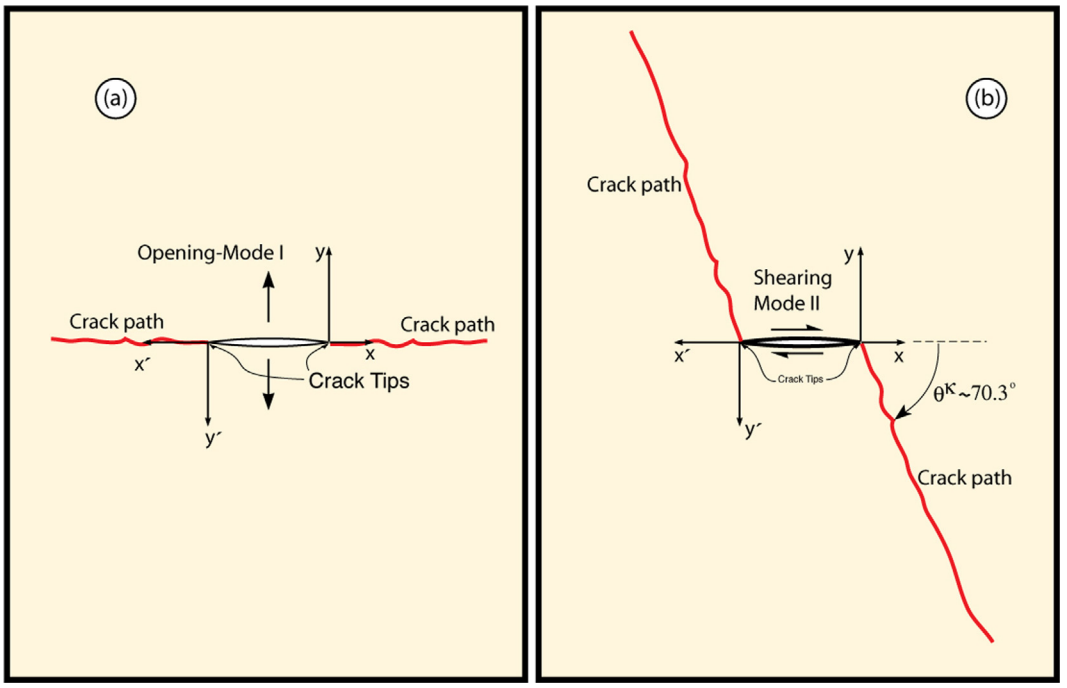

Fig. 1. Schematics showing the likely crack path for the growth of a sharp crack embedded in a homogeneous isotropic system under (a) mode I and (b) mode II loading conditions.

and isotropic systems for which such cracks would be unlikely to form as discussed above, and also possibly due to the complexity of characterizing the mechanics of such a crack.

Driven by the need to design and improve the performance of fiber reinforced and laminate composites wherein fracture may occur along biomaterial interfaces, numerous studies have been conducted in assessing crack growth under, mode I, mixed mode and pure mode II conditions [13–17]. Along the same lines, the study of an embedded horizontal crack such as the case under consideration (see specimen at bottom of Fig. 2) may offer another viable specimen option to study the fracture between two media, homogeneous or heterogeneous, connected through a "third" albeit very thin, interface layer. As has been reported elsewhere, an envelope of material property combinations exists for which a mixed mode or even a pure mode II crack may be forced to propagate along the interface instead of kinking out of plane thus forming a fully embedded macro-mechanical crack of the type considered in this study. Such cracks are often referred to as delamination cracks [5,17–19] which signify a major mode of fracture in composite laminates.

In light of the above, this study aiming at establishing near-tip fracture characteristics of horizontal crack embedded in a cantilever beam under end force conditions, could be used to advance our understanding of mode II interface fracture of similar layers bonded at the interface. The same study can also provide the platform on which further studies can be developed as needed to study delamination in heterogeneous composite laminates while also help advance the state-of-the-art in damage detection model development.

In this work, a J-integral approach [20] is employed in developing estimates of the available elastic energy release rate at the left and right crack tips. In doing so, the cross sectional force and moment resultants and beam deformations such as the slope and deflections at critical sections above and below the crack as well as at the beam's end are used. As discussed in [2,3], estimates of the above quantities can be obtained with the aid of the four-beam model developed in [2]. For that purpose, critical aspects of the model required in the J-integral evaluation shall be summarized first.

2. Summary of the four-beam model

The four-beam model reported in [2,3] yields the resultant forces and moments N_t, V_t, M_t acting at the neutral axis of the beam above the crack and N_b, V_b, M_b acting at the neutral axis of the beam below the crack as shown in Fig. 3. More specifically,

$$M_t = \frac{I_t}{I} M_C \tag{1a}$$

$$M_b = \frac{I_b}{I} M_C \tag{1b}$$

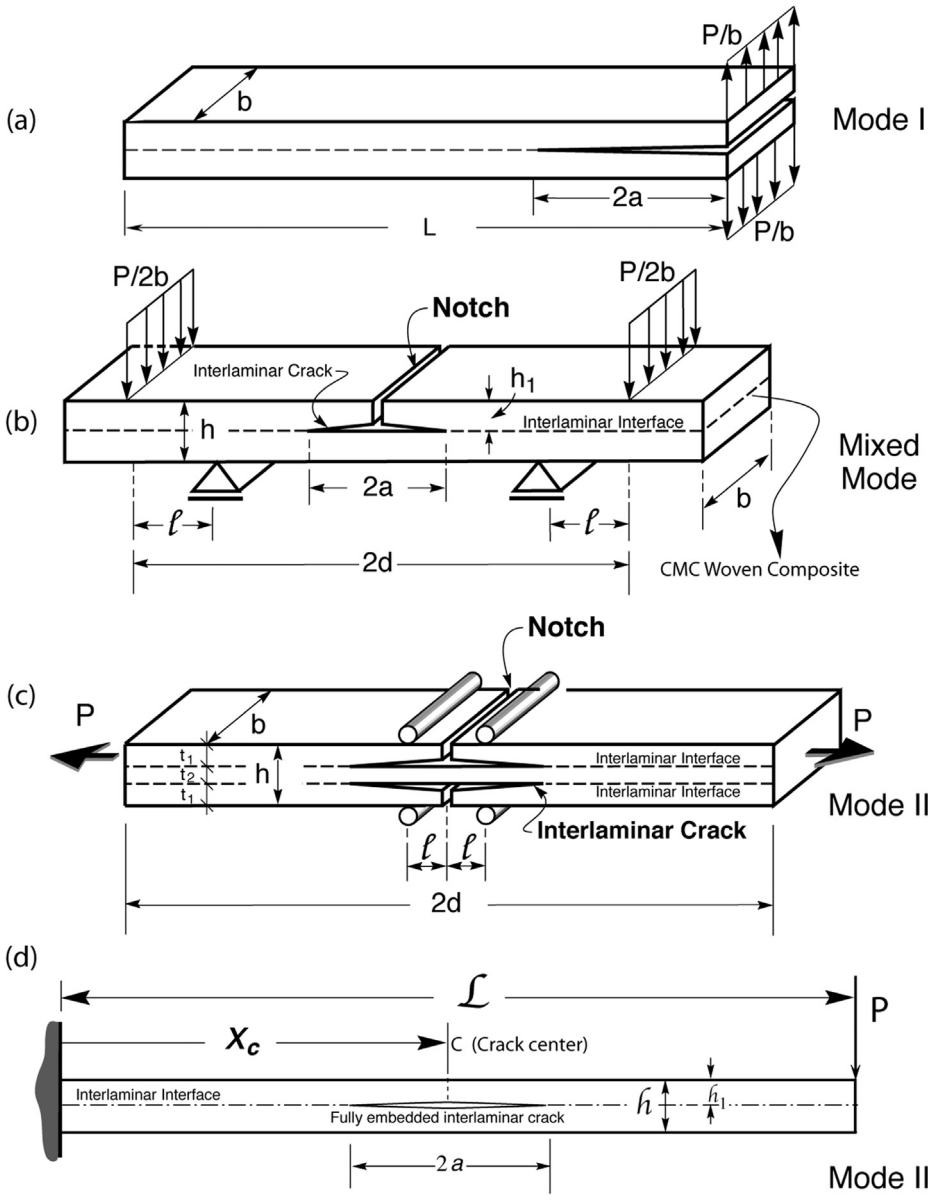

Fig. 2. Schematics of specimens used (a) through (c) in biomaterial fracture under mode I, mixed mode and pure mode II conditions. Specimen shown in (d) is the systems analyzed in [1] and in this study and potentially presents yet another mode II test specimen.

$$N_t = -N_b = -\frac{2M_C}{h}\left(1 - \frac{I_t}{I} - \frac{I_b}{I}\right) \tag{1c}$$

$$V_t = \frac{\gamma I_t}{\gamma I_t + I_b} P \tag{1d}$$

$$V_b = \frac{I_b}{\gamma I_t + I_b} P \tag{1e}$$

where I, I_t, I_b are the second moments of inertia with respect to the neutral axis of the healthy beam, the top beam (beam above the crack), and the bottom beam (beam below the crack), respectively; P is the transverse load applied at the free end; M_C is the bending moment acting at the crack center cross section in the "healthy" beam, i.e., an identical beam without a crack, given by $M_C = -P(L - x_C)$. The parameter γ is a dimensionless quantity related to transition region length λ as dis-

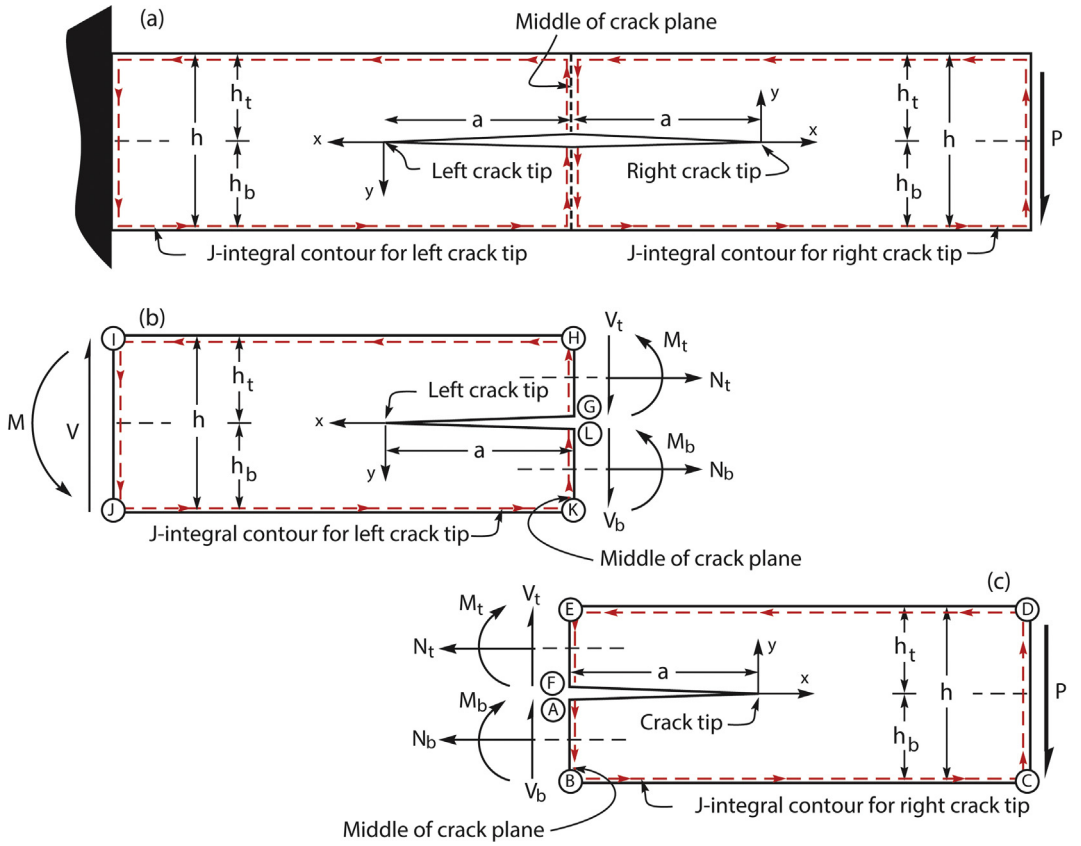

Fig. 3. A schematic of the cantilever beam modeled in this study along with the contour profiles used to evaluate the J-integral for the left and right crack tips shown in (b) and (c) respectively.

cussed in [2]. The Timoshenko constant for the top beam is denoted as k_t and in the bottom beam as k_b. For simplicity, assuming that the transition region length is zero, i.e., $\lambda = 0$, then the parameter γ takes the form,

$$\gamma(\lambda) = \frac{\frac{2}{3} + \frac{1+\nu}{3k_b}\left(\frac{h_b}{a}\right)^2}{\frac{2}{3} + \frac{1+\nu}{3k_t}\left(\frac{h_t}{a}\right)^2} \tag{2}$$

where a is the half crack length; h_t and h_b are height of the top and bottom beams respectively, with the total beam height being $h = h_t + h_b$. Again, using the four-beam model developed in [2,3], the rotations at critical cross sections of the cracked beam are,

$$\varphi_t = \frac{P(L-x_C)a}{EI} - \frac{\gamma P a^2}{2E(\gamma I_t + I_b)} - \frac{P(L-l_1)l_1}{EI} - \frac{Pl_1^2}{2EI} \tag{3a}$$

$$\varphi_b = \frac{P(L-x_C)a}{EI} - \frac{Pa^2}{2E(\gamma I_t + I_b)} - \frac{P(L-l_1)l_1}{EI} - \frac{Pl_1^2}{2EI} \tag{3b}$$

$$\varphi_{end} = -\frac{PL^2}{2EI} \tag{3c}$$

where φ_t and φ_b are the rotation or beam slope of the section through the crack center in the top and bottom beams respectively while φ_{end} is the rotation of the section at the free end of the cantilever beam with $l_1 = x_C - a$.

Note that when incorporating the Timoshenko shear effects, the above expressions are slightly augmented and take the form,

$$\vartheta_t = \varphi_t + \Delta\varphi_t = \varphi_t - \frac{V_t}{k_t A_t G} = \varphi_t - \frac{P}{k_t A_t G}\left(\frac{\gamma I_t}{\gamma I_t + I_b}\right) \tag{4a}$$

$$\vartheta_b = \varphi_b + \Delta\varphi_b = \varphi_b - \frac{V_b}{k_b A_b G} = \varphi_b - \frac{P}{k_b A_b G}\left(\frac{I_b}{\gamma I_t + I_b}\right) \tag{4b}$$

$$\vartheta_{end} = \varphi_{end} + \Delta\varphi_{end} = \varphi_{end} - \frac{P}{kAG} \tag{4c}$$

where k, k_t, k_b are the Timoshenko constants as before and A, A_t, A_b are the cross-sectional areas for the corresponding beams.

In addition, the deflection at the free end of the cracked beam predicted by the four-beam model is given by,

$$\begin{aligned}\delta_{end} = &-\frac{PL^3}{EI}\left\{\frac{1}{3}\hat{l}_1^3 + \frac{1}{2}(1-\hat{l}_1)\hat{l}_1^2 + \frac{(\hat{l}_1+\hat{l}_3)(1+\nu)}{6k}\left(\frac{h}{L}\right)^2 + \left[\frac{1}{2}\hat{l}_1^2 + (1-\hat{l}_1)\hat{l}_1\right](1-\hat{l}_1)\right\}\\ &-\frac{PL^3}{EI}\left\{(1-\hat{x}_C)\hat{a}^2(2+4\lambda+\lambda^2) + \frac{V_t}{P}\frac{I}{I_t}\hat{a}^3\left[\frac{2}{3}+\lambda(2+\lambda)\right] + \frac{V_t}{P}\frac{\hat{a}(1+\nu)}{3k_t}\left(\frac{h}{L}\right)^2\frac{h}{h_t}\right\}\\ &-\frac{PL^3}{EI}\left\{\frac{\lambda\hat{a}(1+\nu)}{6k}\left(\frac{h}{L}\right)^2 + (1-\hat{x}_C)2\hat{a}^2(1+\lambda)\hat{l}_3 + \frac{1}{3}\hat{l}_3^3\right\}\end{aligned} \tag{5}$$

In the above equation the $\widehat{()}$ is used to denote non-dimensional quantities with all length quantities normalized by the beam length L. In addition, Eq. (5) involves the transition region length λ which for simplicity in this study it is assumed to be zero. Under the $\lambda = 0$ assumption, the beam deflection equation given above takes the form,

$$\begin{aligned}\delta_{end} = &-\frac{PL^3}{EI}\left\{\frac{1}{3}\hat{l}_1^3 + \frac{1}{2}(1-\hat{l}_1)\hat{l}_1^2 + \frac{(\hat{l}_1+\hat{l}_3)(1+\nu)}{6k}\left(\frac{h}{L}\right)^2 + \left[\frac{1}{2}\hat{l}_1^2 + (1-\hat{l}_1)\hat{l}_1\right](1-\hat{l}_1)\right\}\\ &-\frac{PL^3}{EI}\left\{2(1-\hat{x}_C)\hat{a}^2 + \frac{2V_t}{3P}\frac{I}{I_t}\hat{a}^3 + \frac{V_t}{P}\frac{\hat{a}(1+\nu)}{3k_t}\left(\frac{h}{L}\right)^2\frac{h}{h_t} + 2(1-\hat{x}_C)\hat{l}_3\hat{a} + \frac{1}{3}\hat{l}_3^3\right\}\end{aligned} \tag{6}$$

where the normalized lengths $\hat{l}_1 = \hat{x}_C - \hat{a}$ and $\hat{l}_3 = 1 - (\hat{x}_C + \hat{a})$, and the other normalized quantities are given in Eqs. (1) and (2).

With the above four-beam model results summarized, we shall now proceed to evaluate the J-integral for the left and right crack tips.

2.1. J-integral evaluation

It is well established [20] that for a linear, elastic and isotropic system, the path independent J-integral [20] is equal to the elastic energy release rate made available to the crack-tip contained within the domain bounded by the J-integral contour Γ and the traction free crack surfaces. Given the path independence of the J-integral, convenient contours Γ for the left Γ_l, and right Γ_r, crack tips are used as shown in Fig. 3. As shown in Fig. 3, each contour initiates at the bottom crack surface relative to a local system placed at the crack tip, and follows the specimen contour in a counter clockwise direction ending at the top crack surface. Accordingly, the contour used in evaluated the J-integral for the left crack tip shown in Fig. 3b comprises of the following segments, $\Gamma_l = \left\{\overline{GH}, \overline{HI}, \overline{IJ}, \overline{JK}, \overline{KL}\right\}$. Similarly, the contour used to evaluate the J-integral for the right crack tip is $\Gamma_r = \left\{\overline{AB}, \overline{BC}, \overline{CD}, \overline{DE}, \overline{EF}\right\}$.

In accordance with [17], the J-integral evaluated along a contour Γ is given by,

$$J = \int_\Gamma w dy - T_i \frac{\partial u_i}{\partial x} ds \tag{7}$$

For a linear elastic system, the strain energy density w is given by $w = \frac{1}{2}\sigma_{ij}\varepsilon_{ij}$ with σ_{ij}, ε_{ij} being the (ij)th components of the stress and strain tensors respectively, $T_i = \sigma_{ij}n_j$ is the ith component of the traction vector along the contour Γ with n_j being the jth component of the unit vector at the point of interest, u_i being the ith component of the displacement vector at the same point. Also in the above equation, ds denotes an increment along the contour Γ, x is the local coordinate for a right handed system placed at the crack tip. Summation over repeated indices from 1 to 2 is implied for planar problems.

Consistent with Fig 3b and c and Eq. (7), the J-integral for the left crack tip evaluated on Γ_l takes the form

$$J^l = \int_{\Gamma_l} w dy - T_i \frac{\partial u_i}{\partial x} ds = \int_{GH} ds + \int_{HI} ds + \int_{IJ} ds + \int_{JK} ds + \int_{KL} ds \tag{8a}$$

or

$$J^l = J^{GH} + J^{HI} + J^{IJ} + J^{JK} + J^{KL} \tag{8b}$$

Similarly, the J-integral for the right crack is evaluated over five contour segments as follows,

$$J^r = \int_{\Gamma_r} wdy - T_i \frac{\partial u_i}{\partial x} ds = \int_{AB} ds + \int_{BC} ds + \int_{CD} ds + \int_{DE} ds + \int_{EF} ds \tag{9a}$$

or

$$J^r = J^{AB} + J^{BC} + J^{CD} + J^{DE} + J^{EF} \tag{9b}$$

It can easily be shown, i.e., due to traction free surfaces and $dy = 0$, that no contribution is made to the J-integral along the top and bottom horizontal segments $\overline{HI}, \overline{JK}$ for the left crack tip, and $\overline{BC}, \overline{DE}$ for the right crack tip, i.e., $J^{HI} = J^{JK} = J^{BC} = J^{DE} = 0$.

As derived in the Appendix, the contribution to the J-integral along the vertical contour segments $\overline{AB}, \overline{CD}, \overline{EF}$ for the right tip appearing in Eq. (9) are obtained in terms of the resultant forces and moment and beam slope at the reference sections as follows

$$J^{AB} = \frac{M_b^2}{2EI_b} + \frac{N_b^2}{2EA_b} - \vartheta^b V_b \tag{10a}$$

$$J^{EF} = \frac{M_t^2}{2EI_t} + \frac{N_t^2}{2EA_t} - \vartheta^t V_t \tag{10b}$$

$$J^{CD} = \vartheta^{end} P \tag{10c}$$

Similarly, the contributions to the J-integral from vertical contour segments $\overline{GH}, \overline{IJ}, \overline{KL}$ for the left tip appearing in Eq. (8) are given by

$$J^{KL} = \frac{M_b^2}{2EI_b} + \frac{N_b^2}{2EA_b} - \vartheta^b V_b \tag{11a}$$

$$J^{GH} = \frac{M_t^2}{2EI_t} + \frac{N_t^2}{2EA_t} - \vartheta^t V_t \tag{11b}$$

$$J^{IJ} = -\frac{M^2}{2EI} - \frac{P^2}{kAG} \tag{11c}$$

In Eqs. (10) and (11), P is the applied force, $M = -PL$ is the bending moment acting at the fixed end of the beam, ϑ denotes the Timoshenko angle at the respective cross sections for the top ϑ^t, and bottom ϑ^b beams respectively; E, G are the modulus of elasticity and shear modulus respectively, whereas I, A represent the 2nd moment of inertia and cross sectional area respectively for the beams indicated by their respective superscript and k is the Timoshenko shear constant. As indicated above, all derivations details for the above equations are presented in the Appendix. With the aid of Eqs. (10) and (11), the following J-integral expressions are obtained for the left and right crack tips.

$$J^l = \frac{M_t^2}{2EI_t} + \frac{N_t^2}{2EA_t} - \vartheta^t V_t + \frac{M_b^2}{2EI_b} + \frac{N_b^2}{2EA_b} - \vartheta^b V_b - \frac{M^2}{2EI} - \frac{P^2}{kAG} \tag{12}$$

At the same time, the right crack tip J-integral takes the form

$$J^r = \frac{M_t^2}{2EI_t} + \frac{N_t^2}{2EA_t} - \vartheta^t V_t + \frac{M_b^2}{2EI_b} + \frac{N_b^2}{2EA_b} - \vartheta^b V_b - \frac{P^2L^2}{2EI} - \frac{P^2}{kAG} \tag{13}$$

When comparing the above two equations, one can easily conclude that,

$$J^r = J^l = \frac{P^2L^2}{Eh^3} 6\hat{a}^2 \left\{ \frac{h^3}{\left(\gamma h_t^3 + h_b^3\right)^2} \left(\gamma^2 h_t^3 + h_b^3\right) - 1 \right\} + \frac{P^2L^2}{Eh^3} \frac{(1+2\nu)}{k} \left(\frac{h}{L}\right)^2 \frac{h_t h_b \left(\gamma h_t^2 - h_b^2\right)^2}{\left(\gamma h_t^3 + h_b^3\right)^2} \tag{14}$$

Let the factor $\Im_c = \frac{P^2L^2}{Eh^3}$ be used as a characteristic energy release rate quantity in non-dimensionalizing the near-tip energy release rate. Since for linear elasticity, $J = \Im$, as the near tip energy release rate, then the non-dimensional energy release rate made available to both the left and right crack tips is given by,

$$\hat{\Im}^{MM} = 6\hat{a}^2 \left\{ \frac{h^3}{\left(\gamma h_t^3 + h_b^3\right)^2} \left(\gamma^2 h_t^3 + h_b^3\right) - 1 \right\} + \frac{(1+2\nu)}{k} \left(\frac{h}{L}\right)^2 \frac{h_t h_b \left(\gamma h_t^2 - h_b^2\right)^2}{\left(\gamma h_t^3 + h_b^3\right)^2} \tag{15}$$

predicted with the aid of the J-integral and the four-beam model [18] established using the Mechanics of Materials (MM) four-beam model. It may be of importance to state that the above non-dimensional expression given by Eq. (15) holds true under both plane stress and plane strain conditions. The distinction between plane stress and plane strain is made through

the characteristic energy release rate $\Im_c = \frac{P^2L^2}{Eh^3}$ by replacing the elastic modulus E with its plane strain equivalent, i.e., $E/(1-\nu^2)$.

In the next section, the compliance method [21–24] is employed in deriving an independent expression for the near tip energy release rate for the cracked system under consideration.

2.2. Compliance method

In accordance with the compliance method, under fixed load conditions, the near-tip energy release rate is given by,

$$\Im^{COMP} = \frac{1}{t}\left(\frac{F^2}{2}\frac{\partial C(l)}{\partial l}\right) \tag{16}$$

where the total applied force at the end of the beam is $F = Pt$, with t being the beam width, and P being the line force acting at the end of the beam across its width. Also in the above expression, $C(l)$ is the beam's compliance relating the deformation at the end of the beam to the applied force such that, $\delta_{end} = C(l)P$. As discussed earlier in this work, the deflection at the free end of the beam is obtained with the aid of the four-beam model [2,3] and can be expressed as,

$$\delta_{end} = \frac{FL^3}{EI}\hat{\delta} \tag{17}$$

with $\hat{\delta}$ being the normalized deflection at the free end given by,

$$\hat{\delta} = -\left\{\frac{1}{3}\hat{l}_1^3 + \frac{1}{2}(1-\hat{l}_1)\hat{l}_1^2 + \frac{(\hat{l}_1+\hat{l}_3)(1+\nu)}{6k}\left(\frac{h}{L}\right)^2 + \left[\frac{1}{2}\hat{l}_1^2 + (1-\hat{l}_1)\hat{l}_1\right](1-\hat{l}_1)\right\}$$
$$-\left\{2(1-\hat{x}_C)\hat{a}^2 + \frac{2V_t}{3P}\frac{I}{I_t}\hat{a}^3 + \frac{V_t}{P}\frac{\hat{a}(1+\nu)}{3k_t}\left(\frac{h}{L}\right)^2\frac{h}{h_t} + 2(1-\hat{x}_C)\hat{l}_3\hat{a} + \frac{1}{3}\hat{l}_3^3\right\} \tag{18}$$

Accordingly, the compliance expressed in terms of the crack length is given by

$$C(l) = \frac{\delta_{end}}{F} = \frac{L^3}{EI}\hat{\delta} \tag{19}$$

and the derivative of the compliance with respect to crack length, i.e., $\frac{\partial C(l)}{\partial l}$ is

$$\frac{\partial C(l)}{\partial l} = \frac{L^3}{EI}\frac{\partial\hat{\delta}}{\partial\hat{a}}\frac{\partial\hat{a}}{\partial\hat{l}}\frac{\partial\hat{l}}{\partial l} = \frac{L^2}{2EI}\frac{\partial\hat{\delta}}{\partial\hat{a}} = \frac{6L^2}{Eth^3}\frac{\partial\hat{\delta}}{\partial\hat{a}} \tag{20}$$

with $\hat{l} = 2\hat{a} = l/L$ and $I = \frac{wh^3}{12}$. With the aid of Eqs. (16), (18) and (20), the energy release rate calculated using the compliance methods takes the form

$$\Im^{COMP} = \frac{P^2L^2}{Eh^3}\frac{\partial\hat{\delta}}{\partial\hat{a}} = \frac{P^2L^2}{Eh^3}\hat{\Im}^{COMP} \tag{21}$$

where $\hat{\Im}^{COMP}$ is the normalized energy release rate obtained using the compliance method and is given by

$$\hat{\Im}^{COMP} = 3\frac{\partial\hat{\delta}}{\partial\hat{a}} \tag{22}$$

$\hat{\Im}^{COMP}$ given by Eq. (22) and $\hat{\Im}^{MM}$ given by Eq. (15) shall now be compared to 2-D FE predictions for a wide range of parameters.

2.3. Finite element modeling

Broad finite element [25] studies of a cantilever beam containing a fully embedded sharp crack and subjected to end transverse loading have been carried out as reported in [1,26]. In those studies, cracks of varying length and orientation were systematically placed at various geometrically admissible locations within the beam. The near-tip energy release rate along with the mode I and mode II stress intensity factors dominating the crack tip regions were extracted and reported in [1]. Independent verification of the FE results was established by solving the same problem using an in-house program as well as the commercially available ABAQUS software [27]. For completeness, specifics of the finite element modeling used in deriving the results reported in this study shall be presented next.

As shown in Figs. 4 and 5, a 2-D rectangular domain of length L and height h with a horizontal sharp crack of length $l = 2a$ with its center located at position x_C from the left fixed end and at depth h_t from the top surface was discretized using 4-noded isoparametric elements under plane stress conditions. A generalized mesh generator developed in [1,26] was used.

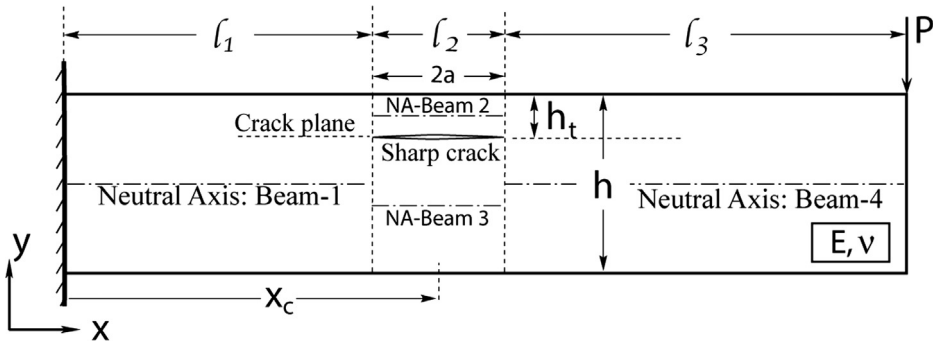

Fig. 4. A schematic of the cracked beam model used in conducting the parametric studies reported in this work. Non-dimensional simulations were conducted using beam length $L = 1$, load $P = 1$, elastic modulus $E = 1$, Poisson's ratio $\nu = 0.3$, aspect ratio $h/L = 0.1, 0.2, 0.05$, half crack length $a/L = 0.05, 0.1, 0.15, 0.2, 0.25$, crack depth $h_t/h = 0.05, 0.1, 0.2, 0.3, 0.4, 0.5, 0.6, 0.7, 0.8, 0.9, 0.95$. The 2-D finite element simulations were conducted under plane stress condition.

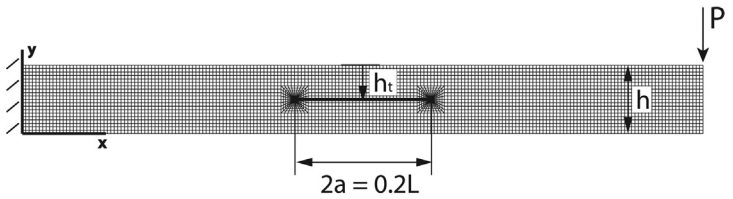

Fig. 5. Two dimensional finite element models used in extracting near-tip energy release rate used in the comparison studies reported in Figs. 6–8 below. As shown, the fixed conditions were imposed on the left edge of the beam whereas a downward transverse load P was applied at the top right corner of each mesh. The models shown represent beams containing horizontal cracks of length $2a = 0.2L$ at various depths h_t/h as described in Fig. 4, with a beam aspect ratio $h/L = 0.1$.

Care was given to the meshing [26,28–30] of the near-tip regions using a converging "spider web" with a minimum of 16 rings of elements all placed within a small region as needed to capture sufficient details of the near-tip singular fields. A vertical transverse load P was applied at the top right corner of the mesh as shown in Figs. 4 and 5. The finite element simulations were carried out in a non-dimensional environment as discussed in [1,26], where the length of the beam L was taken to be the characteristic length, its elastic modulus was taken to be the characteristic modulus with a Poisson's ratio $\nu = 0.3$ and the intensity of the applied load P was taken to be the characteristic line force. Fig. 5 shows a typical FE model in which a crack of length $2a = 0.2L$ is shown to be placed at $x_C = 0.5L$ at depth as measured by the parameter $h_t/h = 0.5$. For this study, only horizontal cracks were modeled. For each FE model, the near-tip energy release rate was extracted using Park's [31,32] stiffness derivative method as well as a numerical implementation of the J-integral. Both methods yielded near-tip energy release rate results that are in excellent agreement as reported in this study and discussed below.

3. Results and discussion

In this section, the effects of crack depth h_t/h, crack length a/L, crack center location (x_C, y_C), and beam aspect ratio h/L, on the near tip energy release rate, are explored through systematics parametric studies. Through these studies, analytical predictions and 2-D finite element results are compared over a broad range of crack depths h_t/h and crack lengths a/L. The analytical predictions were obtained using the J-integral results given by Eq. (15) and the compliance method given by Eq. (22). Both of the above models utilize the four-beam model results and assumed identical Timoshenko constants for all local beams regardless of their aspect ratio, i.e., $k = k_t = k_b = 0.856$, while also ignoring the presence of a transition region [2].

The finite element simulations were conducted using the general methodology described earlier in this study. Systematic parametric studies were conducted in a non-dimensional environment using beam length $L = 1$, load $P = 1$, elastic modulus $E = 1$, Poisson's ratio $\nu = 0.3$. Multiple models for three beam aspect ratios, i.e., $h/L = 0.05, 0.1, 02$ were developed. More specifically, for each aspect ratio considered, FE models for half crack length $a/L = 0.05, 0.1, 0.15, 0.2, 0.25$ were developed with the crack located at different depths as measured by the parameter $h_t/h = 0.05, 0.1, 0.2, 0.3, 0.4, 0.5$ for cracks above or at the mid-plane of the beam, as well as for cracks located below the mid-plane corresponding to $h_t/h = 0.6, 0.7, 0.8, 0.9, 0.95$. In all, 165 FE models were developed and used in conducting the parametric studies reported herein.

For comparison purposes, the reported non-dimensional FE energy release rate values were normalized by the characteristic energy release rate $\mathfrak{I}_c$ given below, consistent with the normalization used earlier in this study, i.e.,

$$\mathfrak{I}_c = \frac{P^2 L^2}{E h^3} \tag{23}$$

In carrying out the parametric FE studies, for a fixed h/L beam aspect ratio and a fixed crack location as measured by its crack center x_c/L and crack depth h_t/h, FE models were developed with each model containing a horizontal crack at progressively larger crack length. The near-tip energy release rate and associated stress intensity factors for both the left and right crack tips were then extracted with the aid of the stiffness derivative method [31,32] and the Crack Surface Displacement (CSD) method [17,15] as reported elsewhere [1,26]. As discussed earlier in this study, the analytical methods used to derive the near-tip energy release rate showed that the energy release rate made available to the left crack tip is equal to its counterpart made available to the right crack tip, i.e., $\mathfrak{I}^{ltp} = \mathfrak{I}^{rtp}$, where the superscripts *ltp* and *rtp* denote the left and right tips respectively. At the same time, slightly different predictions for the left and right tip energy release rates are obtained for the same system using a 2-D finite element model. As such, an average finite element estimate $\mathfrak{I}^{FEavg} = (\mathfrak{I}^{FEltp} + \mathfrak{I}^{FErtp})/2$ is reported for each model in both the tables and figures presented below and used for comparison with the analytical predictions. Thus, the left and right tip average non-dimensional energy release rate finite element predictions obtained for a beam of aspect ratio $h/L = 0.05, 0.1$ and 0.2 are reported.

3.1. Comparisons between FE estimates and analytical J-integral predictions

Results obtained using the FE models discussed above along with related predictions using the models of J-integral and Compliance methods are reported in Table 1 and Figs. 6–8. More specifically, and as shown in Table 1, the results for beam aspect ratio $h/L = 0.05, 0.1$ and 0.2 are reported. For each reported beam aspect ratio, a fixed crack length $a/L = 0.15$ is used for which cracks are placed at different depths as measured by the parameter $h_t/h = 0.05, 0.1, 0.2, 0.3, 0.4, 0.5$. The column under $\mathfrak{I}^{FEavg}$ reports the average J-integral FE estimates obtained for the left and right crack tips. The $\mathfrak{I}^{MM}$ column of results corresponds to estimates obtained using the analytical J-integral given by Eq. (15) whereas the results under the $\mathfrak{I}^{COMP}$ column represent Compliance method estimates obtained with the aid of Eq. (22). The % difference between the FE and MM estimates as well as % difference between the MM and COMP method estimates are reported in Table 1. As shown in Table 1, the MM and COMP method predictions are in excellent agreement to within less than 0.8% for slender beams of aspect ration $h/L \leqslant 0.1$ and to within 3% of each other for a relatively short beam of aspect ration $h/L = 0.2$. Greater deviation is shown to exist between the FE predictions and the MM J-integral estimates. A maximum of about 12% difference is shown to exist for the case of a short beam, i.e., $h/L = 0.2$ and $h_t/h = 0.2$. Interestingly, for the same short beam, the % difference between the FE predictions and the MM J-integral estimates reduces to less than 1% when for a crack placed on the mid-plane of the beam, i.e., $h_t/h = 0.5$. Smaller % difference between the FE results and the MM J-integral model predictions is found to exist for more slender beams, i.e., beams with $h/L \leqslant 0.1$. Based on the results reported in Table 1, one may conclude that the Mechanics of Materials (MM) J-integral predictions and those obtained using the Compliance (COMP) method are almost

Table 1
Numerical results for the non-dimensional energy release rate obtained using 2-D finite elements (FE) with ABAQUS, analytically using J-integral approach (MM), and the compliance method (COMP). The % difference between the FE and MM results as well as between the COMP and MM predictions are also shown. The results reported in this table correspond to those shown in Figs. 6–8 and were obtained for cantilever beams with an embedded horizontal crack of half length $a/L = 0.15$ and subjected to an end transverse load as shown in Fig. 4. Results for beam aspect ratio of $h/L = 0.0.5, 0.1$ and 0.2 with a horizontal crack centered at $x_C = 0.5L$ reported.

h/L	a/L	h_t/h	$\hat{\mathfrak{I}}^{FEavg}$	$\hat{\mathfrak{I}}^{MM}$	$\hat{\mathfrak{I}}^{COMP}$	% diff. [a] (FEavg-MM)	% diff. [b] (COMP-MM)
0.05	0.15	0.05	0.0214	0.0227	0.0226	−5.73	−0.20
0.05	0.15	0.10	0.0495	0.0504	0.0503	−1.79	−0.19
0.05	0.15	0.20	0.1277	0.1256	0.1254	1.67	−0.15
0.05	0.15	0.30	0.2329	0.2310	0.2308	0.82	−0.09
0.05	0.15	0.40	0.3425	0.3477	0.3476	−1.50	−0.03
0.05	0.15	0.50	0.3908	0.4050	0.4050	−3.51	0.00
0.1	0.15	0.05	0.0231	0.0234	0.0232	−1.28	−0.78
0.1	0.15	0.10	0.0547	0.0520	0.0516	5.19	−0.72
0.1	0.15	0.20	0.1429	0.1286	0.1279	11.12	−0.56
0.1	0.15	0.30	0.2584	0.2345	0.2337	10.19	−0.34
0.1	0.15	0.40	0.3720	0.3495	0.3491	6.44	−0.11
0.1	0.15	0.50	0.4220	0.4050	0.4050	4.20	0.00
0.2	0.15	0.05	0.0234	0.0264	0.0256	−11.29	−2.76
0.2	0.15	0.10	0.0586	0.0581	0.0566	0.98	−2.53
0.2	0.15	0.20	0.1586	0.1409	0.1383	12.59	−1.86
0.2	0.15	0.30	0.2831	0.2488	0.2463	13.77	−1.03
0.2	0.15	0.40	0.3927	0.3565	0.3555	10.15	−0.29
0.2	0.15	0.50	0.4376	0.4050	0.4050	8.04	0.00

[a] $\%\ diff_{FEavg-MM} = \frac{\hat{\mathfrak{I}}^{FEavg} - \hat{\mathfrak{I}}^{MM}}{\hat{\mathfrak{I}}^{MM}} \times 100\%$.

[b] $\%\ diff_{COMP-MM} = \frac{\hat{\mathfrak{I}}^{COMP} - \hat{\mathfrak{I}}^{MM}}{\hat{\mathfrak{I}}^{MM}} \times 100\%$.

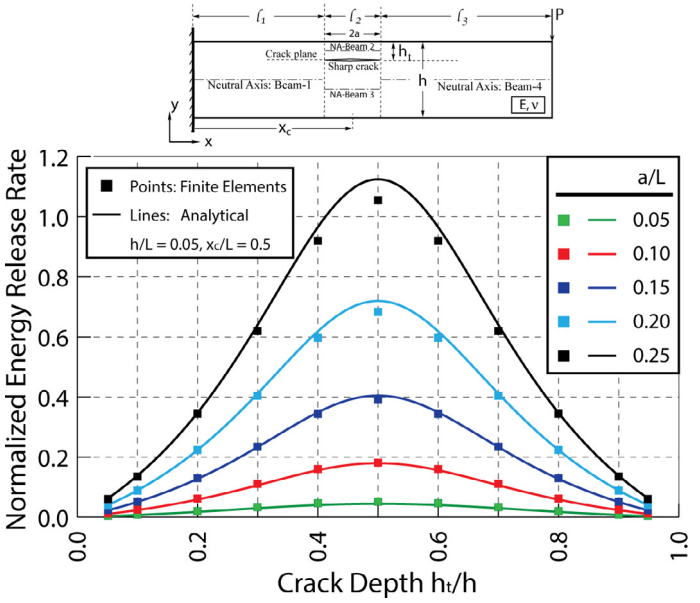

Fig. 6. Normalized energy release rate predictions plotted against the normalized crack depth h_t/h. The discrete points represent 2-D FE estimates whereas the solid lines represent analytical estimates obtained using the J-integral method. Different colors were used to represent systems containing a horizontal crack of different length as indicated. The simulations were conducted under plane stress conditions for a beam of aspect ratio $h/L = 0.05$ and the crack located at $x_C = 0.5L$ along the beam axis.

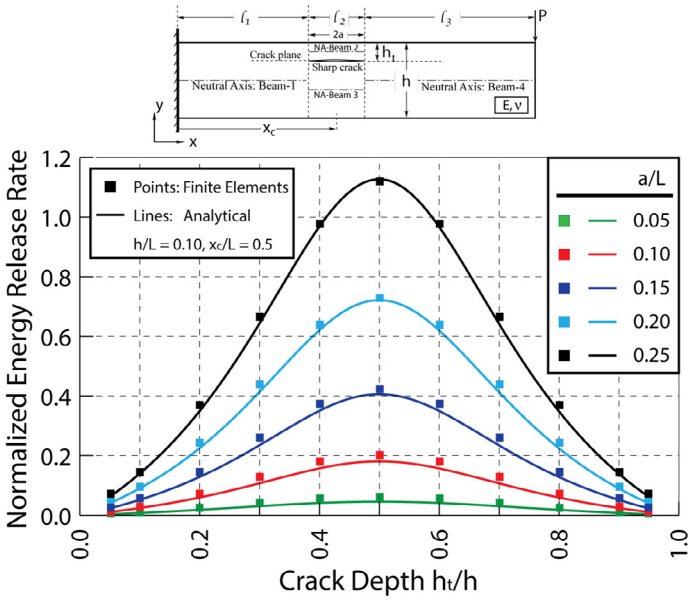

Fig. 7. Normalized energy release rate predictions plotted against the normalized crack depth h_t/h. The discrete points represent 2-D FE estimates whereas the solid lines represent analytical estimates obtained using the J-integral method. Different colors were used to represent systems containing a horizontal crack of different length as indicated. The simulations were conducted under plane stress conditions for a beam of aspect ratio $h/L = 0.1$ and the crack located at $x_C = 0.5L$ along the beam axis.

identical. The small differences reported may be attributed to either numerical error or the Timoshenko shear effects that may be incorporated differentially between the two methods. At the same time, the results predicted by either the J-integral or the Compliance method suggest that the non-dimensional energy release rate is very weakly dependent on the beam aspect ratio h/L, at least for the range of values reported. The higher % difference reported for the FE and the MM J-integral estimates appears to also be related to shear effects. Such effects are expected to be more pronounced in shorter beams, i.e., beams with higher h/L aspect ratio. In addition, based on the four-beam model employed in evaluating

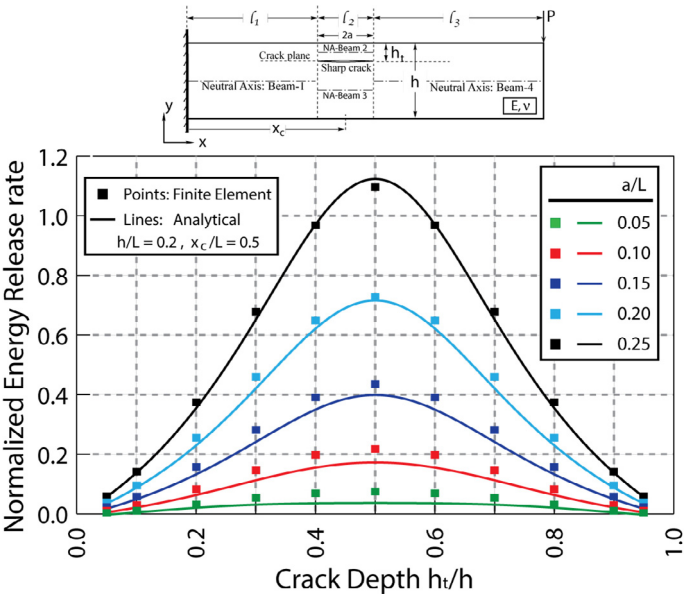

Fig. 8. Normalized energy release rate predictions plotted against the normalized crack depth h_t/h. The discrete points represent 2-D FE estimates whereas the solid lines represent analytical estimates obtained using the J-integral method. Different colors were used to represent systems containing a horizontal crack of different length as indicated. The simulations were conducted under plane stress conditions for a beam of aspect ratio $h/L = 0.2$ and the crack located at $x_C = 0.5L$ along the beam axis.

the J-integral, the aspect ratio of the beams above and below the crack depends on both the crack length and the crack depth. For example, for a beam of a global aspect ratio $h/L = 0.2$, and a crack of half length $a = 0.15L$, placed at depth $h_t/h = 0.2$ would result in Beam-3 [2] below the crack having a local aspect ratio of 0.533 which is a very short beam with a 1 to 2 height to length ratio. In such beams, accounting for shear effects may be of greater importance than it is in otherwise slender beams. As discussed earlier in this study, in the four-beam model, such effects are partially accounted for though a transition region which was neglected in this study.

Given the agreement obtained between the two analytical methods, only the J-integral method results are presented in Figs 6–8 for comparison with the 2-D finite element predictions. As discussed above, J-integral analytical predictions for the non-dimensional energy release rates are plotted in Fig. 6 along with their finite element counterparts, against the normalized crack depth for a relatively slender beam of $h/L = 0.05$ aspect ratio. As shown, the analytical predictions are plotted using solid lines. The same color scheme is used to report finite element and analytical results corresponding to systems with a crack of the same normalized crack length. For example, a green color is used to represent the finite element results shown on discrete points and analytical predictions shown in a green line for systems containing a horizontal crack of normalized half length $a/L = 0.05$. In the same manner, a red color is used to represent the results for systems containing a crack of $a/L = 0.1$, dark blue, light blue and black colors correspond to systems of $a/L = 0.15, 0.2, 0.25$ respectively. It is evident by inspection that the analytical model predictions are in close agreement with their 2-D finite element counterparts over the entire range of h_t/h and a/L parameters used in obtaining the results shown in Fig. 6. Such an agreement reinforces confidence in both the finite element and analytical models and in particular the four-beam model developed in [2,3] which formed the foundation for the J-integral evaluation and compliance method implementation. The results of each curve at certain crack depth suggest that for larger cracks, i.e., $a/L \geqslant 0.15$, an excellent agreement is shown between the analytical and 2-D finite element predictions. This finding is applicable for all crack depths considered. However, with increasing h/L beam aspect ratio, and for smaller cracks, i.e., $a/L \leqslant 0.1$, a slight deviation between the analytical and FE model predictions is observed for cracks located at depths near the neutral axis. Although small, such deviations may be attributed to the analytical model limitations (assuming transition region length parameter $\lambda = 0$), in fully capturing the stress and deformation fields in the near-tip regions as well as in the beams above and below the crack plane which become increasingly stubby beams for short cracks, i.e., $a/L \leqslant 0.1$.

By inspection, Fig. 6 shows that the energy release rates made available to the left and right crack tips of a horizontal crack embedded in a cantilever beam under an end transverse load exhibit a symmetry with respect to the beam neutral axis. Thus, systems containing such a horizontal crack located at symmetrical distances above and below the beam's neutral axis, experience equal amounts of energy release rate at both the left and right crack tips. The results reported in Fig. 6 also suggest that for any given crack length and a specified x_C location, a system with a crack located at the beam's neutral axis induces maximum normalized energy release rate to the crack tip regions when compared to similar systems with the crack located at any other depth. This finding may not be surprising since a mode II crack such as the horizontal cracks considered

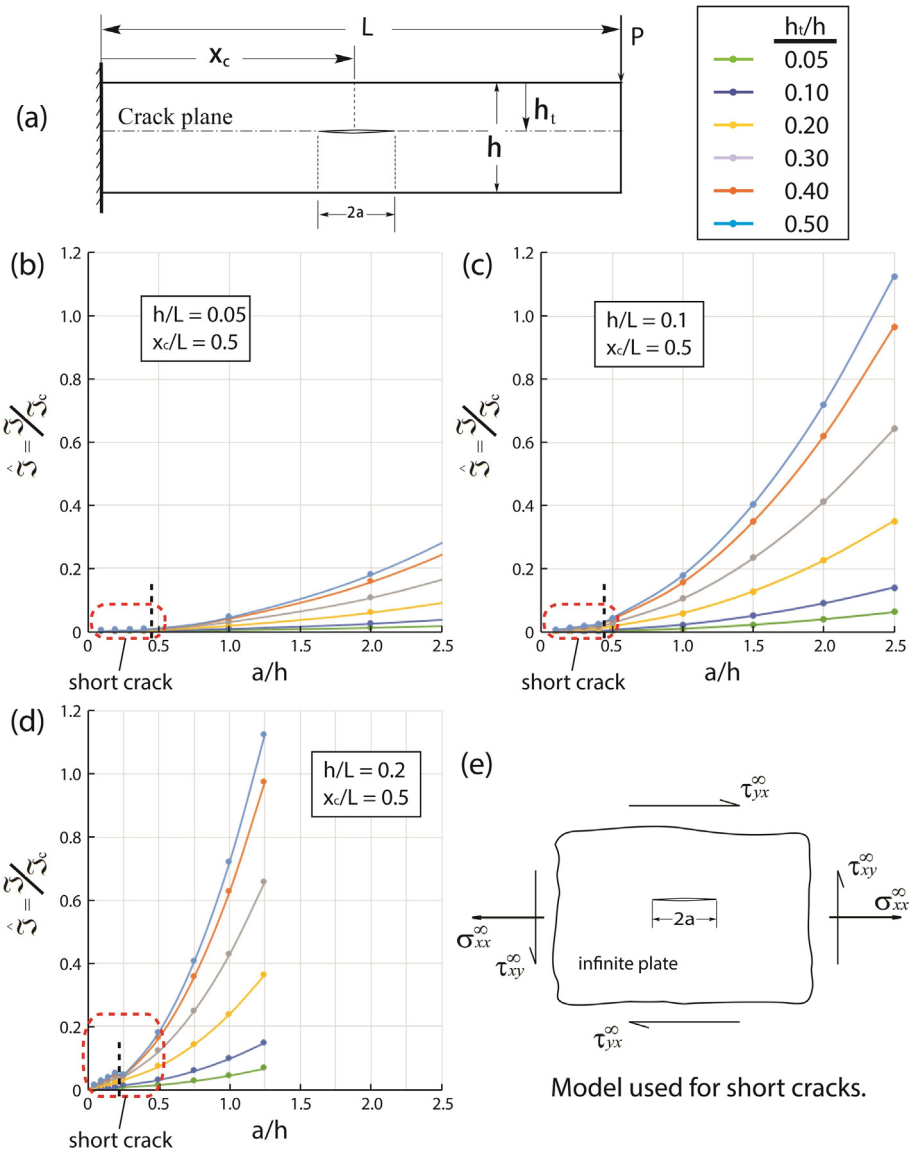

Fig. 9. The normalized energy release rate versus the ratio of the half crack length over the beam height a/h. The first four points close to $a/h = 0$ in each curve were obtained with the aid of the infinite plate model shown schematically in (e) above, while the other points in each curve were obtained using the J-integral model. (a) Schematic of the beam model used in the parametric studies. The crack is placed at $x_C = 0.5L$ along the beam axis. Figures (b), (c) and (d) show the graphs obtained for beams of aspect ratio $h/L = 0.05, 0.1, 0.2$ respectively.

in the study [1] is most sensitive to the remote shear stress which assumes a maximum at the beam's neutral axis. Again, as shown in Fig. 6, the normalized energy release rate is scaled to the maximum energy release rate value exhibited by each curve, and is shown to increase substantially with the normalized half crack length a/L, the effects of which are further explored later on in this section.

Normalized energy release rate predictions similar to those reported in Fig. 6 are also reported in Figs. 7 and 8 for progressively taller beams, i.e., beams of aspect ratio $h/L = 0.1$ for Fig. 7 and $h/L = 0.2$ for Fig. 8. As before, good agreement is shown to exist between the analytical and 2-D finite element predictions. In addition, Figs. 7 and 8 suggest that the normalized energy release rate obtained for increasing taller beams, i.e., $h/L = 0.1$ or 0.2 exhibit similar overall trends to those discussed in association with Fig. 6. More specifically, the normalized energy release rates are shown to be symmetric with respect to the crack location relative to beam's neutral axis, exhibiting a maximum for cracks located at the neutral axis. In addition, the results for all systems reported in Figs. 6–8 suggest that the energy release rate increases monotonically with crack length. It is also remarkable to observe that for the three types of beam systems considered, i.e., slender beams with $h/L = 0.05$, intermediate aspect ratio of $h/L = 0.1$ and relatively tall beams of $h/L = 0.2$, the normalized energy release rates appear to be rather insensitive to the beam aspect ratio with the three system predictions shown to be almost identical for the corresponding crack lengths.

3.2. Comparisons to approximate short crack solutions

In Fig. 9, the energy release rate estimates obtained analytically as discussed above are plotted against a/h for beams of aspect ratio h/L equal to 0.05, 0.1 and 0.2. In all cases reported the crack center was placed at $x_C = 0.5L$. Results for six different h_t/h ratios are reported. Along with the above results, in the same figures the approximate short crack estimates are also reported as needed to further understand the effects of crack length for very small cracks. In doing so, in the case of very small cracks, i.e., $a/h < 0.5$, the fracture conditions in the crack tip region can be approximated using an infinite plate model with a center crack [33,34] of length $2a$ and subjected to remote normal and shear stresses, σ_{xx} and τ_{xy} respectively as shown in Fig. 9. The remotes stress applied to this otherwise "infinite" plate should be those induced by the flexural bending loading, i.e., the normal stress σ_{xx} induced by the bending moment M and the shear stress τ_{xy} induced by the transverse the shear force V at the crack center, i.e.,

$$\sigma_{xx} = \sigma_{xx}^{\infty} = -\frac{My}{I} \tag{24a}$$

$$\tau_{xy} = \tau_{xy}^{\infty} = -\frac{VQ(y)}{It(y)} \tag{24b}$$

where M and V are the resultant bending moment and shear force acting on the section, I is the second moment of inertia of the cross section, y is the distance measured from the beam's neutral axis, $Q(y)$ is the first area moment of the cross-sectional area above or below the position y, and t is the beam width. As discussed elsewhere [1,26], since the horizontal crack behaves more like a pure mode II crack, the normal stress σ_{xx} does not contribute to the near-tip stress intensities while the shear stress τ_{xy} gives rise to a mode II stress intensity factor K_{II} such that,

$$K_{II} = \tau_{xy}^{\infty}\sqrt{\pi a} \tag{25}$$

Under mode II conditions, the energy release rate obtained using the infinite plate short crack approximation is then obtained as follows,

$$\Im = \frac{1}{E}K_{II}^2 = \frac{1}{E}(\tau_{xy}^{\infty})^2\pi a \tag{26}$$

Eqs. (24b) and (26) can then be combined to yield the energy release rate in terms of the applied loading, beam geometry and crack location. Such short crack energy release rate estimates normalized by the factor $\Im_c$ were obtained and plotted in Fig. 9 at the lower a/L range denoted as "short crack" solutions. As shown, the latter short crack estimates follow trends consistent with the J-integral estimates which further validates the overall approach employed in this study in establishing the near-tip mechanics of such cracked cantilever beams.

4. Rotary spring stiffness based on J-integral estimates

Rotary springs were introduced in [2,26] in the development of the four-beam model as a means of accounting for the transition regions and added compliance induced by the presence of the horizontal crack. In [2], the effective rotary spring stiffness was obtained using compatibility conditions as well as beam model and finite element deflection matching conditions. In this section, an alternative method is proposed that would enable the determination of the rotary spring stiffnesses using an energy approach.Following the methodology described in the previous section, the change of energy due to the introduction of the crack can be calculated as,

$$\begin{aligned} \Delta\Phi^{left}(a,P)^{\text{Change due to crack}} &= -w\int_{l=-a}^{a}(\Im^{left}(l))_q dl \quad \text{For left beam} \\ \Delta\Phi^{right}(a,P)^{\text{Change due to crack}} &= -w\int_{l=-a}^{a}(\Im^{right}(l))_q dl \quad \text{For right beam} \end{aligned} \tag{27}$$

where the energy release rate $\Im^{left} = J^l$ with J representing the J-integral evaluated along a contour Γ as shown in Fig. 3a and c and is given by [20]

$$J = \int_{\Gamma} w dy - T_i\frac{\partial u_i}{\partial x}ds \tag{28}$$

In the above J-integral expression, w denotes the strain energy density at the point of interest, T_i is the ith traction component given in terms of the stress tensor $[\sigma_{ij}]$ and the unit normal vector n_j such that $T_i = \sigma_{ij}n_j$ with the indices i, j taking on the values 1, 2, 3 and the repeated index j implying summation from 1 to 3. Also in the above equation, u_i represents the ith component of the elastic displacement vector. When evaluating the J-integral along the left and right contours, the following equations are obtained,

$$J^l = \frac{M_b^2}{2EI_b} + \frac{N_b^2}{2EA_b} + \varphi_b^{cr}V_b + \frac{M_t^2}{2EI_t} + \frac{N_t^2}{2EA_t} + \varphi_t^{cr}V_t - \frac{M_{wall}^2}{2EI} \tag{29a}$$

$$J^r = \frac{M_b^2}{2EI_b} + \frac{N_b^2}{2EA_b} + \varphi_b^{cr} V_b + \frac{M_t^2}{2EI_t} + \frac{N_t^2}{2EA_t} + \varphi_t^{cr} V_t - \varphi_{end} P \tag{29b}$$

More expanded forms of the J-integral equations given above are reported earlier in this study. Analytically obtained results using the above equations are presented in Figs. 7–9 where they are also compared to FE results obtained using both an in-house FE algorithm and the ABAQUS software [27]. As discussed earlier in this study, the analytical results are shown to be in remarkable agreement with their FE counterparts for a broad range of cracks lengths and crack depth location.Having established the J-integral through Eq. (29), the additional rotations caused by the presence of the crack can be obtained as follows [33,34]

$$\varphi = \frac{\partial}{\partial P}(\Delta\Phi)\frac{1}{\frac{\partial M}{\partial P}} = \frac{\partial}{\partial P}\left[\int_0^l J(l)dl\right]\frac{1}{\frac{\partial M}{\partial P}} \tag{30}$$

where $M = M^{left}$ or $M = M^{right}$ for the left and right crack tips. Since the rotary spring stiffnesses are linearly related to the additional rotation φ^{left} and φ^{right}, and their work conjugate cross-sectional moments $M^{left} = -P(L-(x_C-a))$ for the left tip and $M^{right} = -P(L-(x_C+a))$ for the right crack tip, the respective rotary spring compliances can then be obtained as follows,

$$C^{left} = \frac{\partial \varphi^{left}}{\partial P}\frac{1}{\frac{\partial M^{left}}{\partial P}} \text{ and } C^{right} = \frac{\partial \varphi^{right}}{\partial P}\frac{1}{\frac{\partial M^{right}}{\partial P}} \tag{31}$$

In our preliminary studies, the above compliances and reciprocal spring stiffness were determined for several crack locations and specimen geometries and were then used to establish the modal response of the four-beam model as discussed in [35,36].

5. Conclusions

In this study, the elastic energy release rate associated with the left and right crack tips of a horizontal crack embedded in a cantilever beam under an end force loading condition has been established analytically and numerically via the method of finite elements. Analytical near-tip energy release rate expressions were developed with the aid of the J-integral and independently using the compliance method. Both methods resulted in identical energy release rate predictions with the left and right crack tips experiencing identical levels of energy release rate. In parallel studies, 2-D finite element models were developed and used to extract the associated energy release rates for a broad range of beam and crack systems. Comparison studies presented in tables and in figures showed remarkable agreement between the analytical and finite element predictions for most models considered. Slight deviations were shown to exist between the two model predictions for short cracks deeply embedded close to the beam's neutral axis. In those cases, an alternative analytical short crack method was considered with the crack embedded in an otherwise infinite plate remotely loaded by the transverse shear and normal bending stresses acting at the center of the crack in an otherwise healthy beam. The results show good agreement with the previous J-integral analytical predictions in the short to long crack length transition region of $a/h \approx 0.5$ (see Fig. 9).

For all systems considered, the energy release rate made available to the left and crack tips was shown to be symmetric with respect to the beam's neutral axis suggesting that horizontal cracks placed at equal distance above and below from the beam's neutral axis experience identical energy release rate values. The reported results also showed that the non-dimensional energy release rates show little if any sensitivity to the beam's aspect ratio for the systems considered but exhibited a non-linear and monotonically increasing trend with the half crack length a/L. The model presented herein along with studies reported in [2,3] suggest that the systems considered may be used as a viable specimen for mode II interfacial fracture studies.

Acknowledgements

Support for this work was provided by the University of Maryland, Baltimore County (UMBC), Designated Research Initiative Fund (DRIF), the UMBC Graduate School through a Dissertation Fellowship and the Mechanical Engineering Department at UMBC through Graduate Teaching Assistantship funds.

Appendix A. J-integral evaluation

In the cantilever beam with a horizontal crack embedded subjected to an end transverse force load, the schematic of J-integral at both the left and right tips is shown in Fig. 3. In accordance with Fig. 3b, the J-integral for the left crack tip evaluated on the closed contour Γ_l of G → H → I → J → K → L takes the form

$$J^l = J^{GH} + J^{HI} + J^{IJ} + J^{JK} + J^{KL} \tag{A.1}$$

We shall now proceed to the evaluation of each J-integral contribution appearing in Eq. (8). For example,

$$J^{HI} = \int_{\Gamma_{HI}} W dy - \left(T_1 \frac{\partial u_1}{\partial x} + T_2 \frac{\partial u_2}{\partial x}\right) ds \tag{A.2}$$

where $x - y$ is the local reference system with origin at the crack tip. Based on the local reference system $x - y$ as shown in Fig. 3b, it follows that $dy = 0$, $ds = dx$, resulting in

$$J^{HI} = \int_{x_H}^{x_I} -\left(T_1 \frac{\partial u_1}{\partial x} + T_2 \frac{\partial u_2}{\partial x}\right) dx \tag{A.3}$$

where T_1 and T_2 are the tractions acting on contour Γ at the point of interest. As shown in Fig. A.1, the contour segments $\overline{HI}$ and $\overline{JK}$ run along traction free surfaces, i.e., $T_1 = T_2 = 0$ on $\overline{HI}$ and $\overline{JK}$. It thus follows that along the latter two segments, no contribution is made to the J-integral normal to the edges where the stress components apply. By switching the integral limit and with $\frac{\partial u_1}{\partial x} = 0$ since the stress state is pure shear at the top edge,

$$J^{HI} = \int_{x_I}^{x_H} \sigma_{12} \frac{\partial u_1}{\partial x} dx \tag{A.4}$$

and apparently,

$$J^{JK} = 0 \tag{A.5}$$

Second, at the fixed end in Fig. 3b,

$$J^{IJ} = \int_{\Gamma_{IJ}} W dy - \left(T_1 \frac{\partial u_1}{\partial x} + T_2 \frac{\partial u_2}{\partial x}\right) ds \tag{A.6}$$

Based on the local reference system $x - y$, it gives $ds = dy$, and with the follows

$$T_1 = \sigma_{11} n_1 + \sigma_{12} n_2 = -\sigma_{11} \tag{A.7a}$$

$$T_2 = \sigma_{21} n_1 + \sigma_{22} n_2 = -\sigma_{21} \tag{A.7b}$$

$$W = \frac{1}{2} \sigma_{ij} \varepsilon_{ij} = \frac{1}{2} (\sigma_{11} \varepsilon_{11} + 2\sigma_{12} \varepsilon_{12}) \tag{A.7c}$$

$$\varepsilon_{12} = \frac{1}{2} \left(\frac{\partial u_1}{\partial y} + \frac{\partial u_2}{\partial x}\right) \tag{A.7d}$$

where u_1 and u_2 are the displacement components at the fixed end (the segment $\overline{IJ}$) in Fig. 3b of the beam in x and y directions respectively. When deforming, the horizontal displacement component, as shown in Fig. A.1, is

$$u_1 = u_1^0 - \vartheta y \tag{A.8}$$

where u_1^0 is constant, ϑ is the slope at the fixed end, such as

$$\vartheta = \varphi + \Delta\varphi \tag{A.9}$$

where $\varphi = 0$ at the fixed end, and $\Delta\varphi = -\frac{V}{kAG} = -\frac{P}{kAG}$. With $\frac{\partial u_1}{\partial y} = -\vartheta$ and $\frac{\partial u_2}{\partial y} = \vartheta$, Eqs. (A.6) and (A.9) yield,

$$J^{IJ} = -\frac{1}{2} \int_{y_j}^{y_I} \sigma_{11} \varepsilon_{11} dy + (-\vartheta) \int_{y_j}^{y_I} \sigma_{12} dy = -\frac{M^2}{2EI} - \frac{P^2}{kAG} \tag{A.10}$$

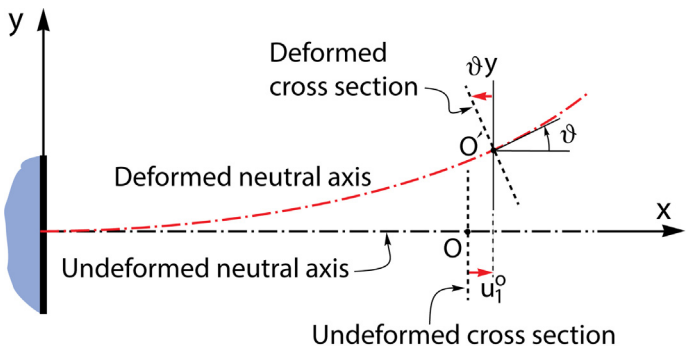

Fig. A.1. A schematic of the horizontal displacement component when the beam is deformed.

Next, the focus is moved to the J-integral at the right edges, i.e., the contour segments $\overline{GH}$ and $\overline{KL}$ as shown in Fig. 3b. For the segment $\overline{GH}$

$$J^{GH} = \int_{\Gamma_{GH}} W dy - \left(T_1 \frac{\partial u_1}{\partial x} + T_2 \frac{\partial u_2}{\partial x}\right) ds \tag{A.11}$$

Based on the local reference system $x - y$, it gives $ds = -dy$ and with the follows

$$T_1 = \sigma_{11} n_1 + \sigma_{12} n_2 = \sigma_{11} \tag{A.12a}$$

$$T_2 = \sigma_{21} n_1 + \sigma_{22} n_2 = \sigma_{21} \tag{A.12b}$$

$$W = \frac{1}{2}\sigma_{ij}\varepsilon_{ij} = \frac{1}{2}(\sigma_{11}\varepsilon_{11} + 2\sigma_{12}\varepsilon_{12}) \tag{A.12c}$$

$$\varepsilon_{12} = \frac{1}{2}\left(\frac{\partial u_1}{\partial y} + \frac{\partial u_2}{\partial x}\right) \tag{A.12d}$$

Eq. (A.11) yields

$$J^{GH} = \int_{y_G}^{y_H} \frac{1}{2}\sigma_{11}\varepsilon_{11} dy + \int_{y_G}^{y_H} \sigma_{12}\left(-\frac{1}{2}\frac{\partial u_1^t}{\partial y} + \frac{1}{2}\frac{\partial u_2^t}{\partial x}\right) dy \tag{A.13}$$

where u_1^t and u_2^t are the displacement components in the top beam in x and y direction respectively. When deforming, the horizontal displacement component at the free end of the top beam is similar to the expression in Eq. (A.8), such that

$$u_1^t = u_1^{t0} - \vartheta^t y \tag{A.14}$$

where u_1^{t0} is constant, ϑ^t is the slope at $\overline{GH}$. With $\frac{\partial u_1^t}{\partial y} = -\vartheta^t$ and $\frac{\partial u_2^t}{\partial y} = \vartheta^t$, Eqs. (A.13) and (A.14) give

$$J^{GH} = \int_{y_G}^{y_H} \frac{1}{2}\sigma_{11}\varepsilon_{11} dy + \vartheta^t \int_{y_G}^{y_H} \sigma_{12} dy = \frac{M_t^2}{2EI_t} + \frac{N_t^2}{2EA_t} - \vartheta^t V_t \tag{A.15}$$

For the segment $\overline{KL}$ in the bottom beam, follow the same procedure, we have

$$J^{KL} = \frac{M_b^2}{2EI_b} + \frac{N_b^2}{2EA_b} - \vartheta^b V_b \tag{A.16}$$

Substituting Eqs. (A.4), (A.5), (A.10), (A.15) and (A.16) into Eq. (A.1), the J-integral in the left part is given by

$$J^l = \frac{M_t^2}{2EI_t} + \frac{N_t^2}{2EA_t} - \vartheta^t V_t + \frac{M_b^2}{2EI_b} + \frac{N_b^2}{2EA_b} - \vartheta^b V_b - \frac{M^2}{2EI} - \frac{P^2}{kAG} \tag{A.17}$$

As to the J integral for the right part, the derivation of solution is similar to that for the left part. With the definition of quantities shown in Fig. 3c, and the closed path Γ_r of A → B → C → D → E → F, it gives

$$J^r = J^{AB} + J^{BC} + J^{CD} + J^{DE} + J^{EF} \tag{A.18}$$

The expressions of each J-integral components in the right part are determined as such

$$J^{AB} = J^{KL} \tag{A.19}$$

$$J^{EF} = J^{GH} \tag{A.20}$$

$$J^{BC} = J^{DE} = 0 \tag{A.21}$$

and the J-integral at the free end (the segment $\overline{CD}$ as shown in Fig. 3c) is

$$J^{CD} = \int_{\Gamma_{CD}} W dy - \left(T_1 \frac{\partial u_1}{\partial x} + T_2 \frac{\partial u_2}{\partial x}\right) ds \tag{A.22}$$

Based on the local reference system $x - y$ shown in Fig. 3c, it gives $ds = dy$. With the follows

$$T_1 = \sigma_{11} n_1 + \sigma_{12} n_2 = 0 \tag{A.23a}$$

$$T_2 = \sigma_{21} n_1 + \sigma_{22} n_2 = \sigma_{21} \tag{A.23b}$$

$$W = \frac{1}{2}\sigma_{ij}\varepsilon_{ij} = \frac{1}{2}(\sigma_{11}\varepsilon_{11} + 2\sigma_{12}\varepsilon_{12}) \tag{A.23c}$$

$$\varepsilon_{12} = \frac{1}{2}\left(\frac{\partial u_1}{\partial y} + \frac{\partial u_2}{\partial x}\right) \tag{A.23d}$$

Eq. (A.22) yields

$$J^{CD} = \frac{1}{2}\int_{y_C}^{y_D} \sigma_{12}\left(\frac{\partial u_1}{\partial y} - \frac{\partial u_2}{\partial x}\right) dy \tag{A.24}$$

When deforming, the horizontal displacement component at the free end is

$$u_1 = u_1^0 - \vartheta_{end} y \tag{A.25}$$

where u_1^0 is constant, ϑ_{end} is the slope at the free end. With $\frac{\partial u_1}{\partial y} = -\vartheta_{end}$ and $\frac{\partial u_2}{\partial x} = \vartheta_{end}$, Eq. (A.24) gives

$$J^{CD} = -\vartheta_{end}\int_{y_C}^{y_D} \sigma_{12} dy = \vartheta_{end} P \tag{A.26}$$

Substituting Eqs. (A.19)–(A.21) and (A.26) into Eq. (A.18), it gives the resultant J-integral for the right crack tip as

$$J^r = \frac{M_t^2}{2EI_t} + \frac{N_t^2}{2EA_t} - \vartheta^t V_t + \frac{M_b^2}{2EI_b} + \frac{N_b^2}{2EA_b} - \vartheta^b V_b - \frac{P^2L^2}{2EI} - \frac{P^2}{kAG} \tag{A.27}$$

Compare Eqs. (A.17) and (A.27), and note that the resistant bending moment $M = PL$ at the fixed end, and the expressions for each normal, shear, and bending moment components, such as N_t, V_t, M_t and N_b, V_b, M_b, that have been discussed elsewhere, we conclude that

$$J^r = J^l = \frac{P^2L^2}{Eh^3} 6\hat{a}^2 \left\{ \frac{h^3}{\left(\gamma h_t^3 + h_b^3\right)^2}\left(\gamma^2 h_t^3 + h_b^3\right) - 1 \right\} + \frac{P^2L^2}{Eh^3}\frac{(1+2\nu)}{k}\left(\frac{h}{L}\right)^2 \frac{h_t h_b \left(\gamma h_t^2 - h_b^2\right)^2}{\left(\gamma h_t^3 + h_b^3\right)^2} \tag{A.28}$$

where γ is shows in Eq. (2), such that

$$\gamma(\lambda) = \frac{\frac{2}{3} + \frac{1+\nu}{3k_b}\left(\frac{h_b}{a}\right)^2}{\frac{2}{3} + \frac{1+\nu}{3k_t}\left(\frac{h_t}{a}\right)^2}$$

Eq. (A.28) evidently shows the components of J-integral at each crack tip. The first term is from resultant bending moments and normal forces, while the second term is associated with shear effects. In Eq. (A.28), the dimensional factor is $\frac{P^2L^2}{Eh^3}$, in units of force per length. The components next to the dimensional factor are dimensionless. Since the energy release rate equals to J-integral in linear theory, the components

$$\hat{\Im} = 6\hat{a}^2 \left\{ \frac{h^3}{\left(\gamma h_t^3 + h_b^3\right)^2}\left(\gamma^2 h_t^3 + h_b^3\right) - 1 \right\} + \frac{(1+2\nu)}{k}\left(\frac{h}{L}\right)^2 \frac{h_t h_b \left(\gamma h_t^2 - h_b^2\right)^2}{\left(\gamma h_t^3 + h_b^3\right)^2} \tag{A.29}$$

will be used as the normalized energy release rate, calculated from the J-integral.

References

[1] Fang X, Charalambides PG. The fracture mechanics of cantilever beams with an embedded sharp crank under end force loading. Eng Fracture Mech 2015;149:1–17.
[2] Charalambides PG, Fang X. The mechanics of a cantilever beam with an embedded horizontal crack subjected to an end transverse force. Part A modeling. Mech, Mater Sci Eng J 2016;5:131–56.
[3] Charalambides PG, Fang X. The mechanics of a cantilever beam with an embedded horizontal crack subjected to an end transverse force. Part B results and discussion. Mech, Mater Sci Eng J 2016;5:157–75.
[4] Evans AG, He MY, Hutchinson JW. Interface debonding and fiber cracking in brittle matrix composites. J Am Ceram Soc 1989;72(12):2300–3.
[5] Charalambides PG. Steady-state mechanics of delamination cracking in laminated ceramic-matrix composites. J Am Ceram Soc 1991;74(12):3066–680.
[6] Charalambides PG, Evans AG. Debonding properties of residually stressed brittle-matrix composites. J Am Ceram Soc 1989;72(5):746–53.
[7] Charalambides PG. Fiber debonding in residually stressed brittle matrix composites. J Am Ceram Soc 1990;73(6):1674–80.
[8] Hartranft RJ, Sih GC. Alternating method applied to edge and surface crack problems. NASA-CR-140846; 1972.
[9] Jin ZH, Batra RC. Stress intensity relaxation at the tip of an edge crack in a functionally graded material subjected to a thermal shock. J Therm Stresses 1996;19(4):317–39.
[10] Chatterjee A. Nonlinear dynamics and damage assessment of a cantilever beam with breathing edge crack. J Vib Acoustics 2011;133(5):051004-1–4-6.
[11] Hall KJ, Potirniche GP. A three-dimensional edge-crack finite element for fracture mechanics applications. Int J Solids Struct 2012;49(2):328–37.
[12] Charalambides PG, Cao HC, Lund J, Evans AG. Development of a test method for measuring the mixed mode fracture resistance of bimaterial interfaces. Mech Mater 1990;8:269–83.
[13] Matos PPL, McMeeking RM, Charalambides PG, Drory MD. A method for calculating stress intensities in bimaterial fracture. Int J Fracture 1989;40:235–54.
[14] Hutchinson JW, Suo Z. Mixed-mode cracking in layered materials. Adv Appl Mech 1992;29:63–191.
[15] Charalambides PG, Zhang W. An energy method for calculating the stress intensities in orthotropic biomaterial fracture. Int J Fracture 1996;76:97–120.
[16] Matsumto T, Tanaka M, Obara Ryo. Computation of stress intensity factors of interface cracks based on interaction energy release rates and BEM sensitivity analysis. Eng Fracture Mech 2000;65(6):683–702.

[17] Charalambides PG, Lund J, Evans AG, McMeeking RM. A test specimen for determining the fracture resistance of bimaterial interfaces. J Appl Mech 1989;56(1):77–82.
[18] Cox BN. Constitutive model for a fiber tow bridging a delamination crack. Mech Compos Mater Struct 1999;6(2):117–38.
[19] Hojo M. Delamination fatigue crack growth in unidirectional graphite/epoxy laminates. J Reinforced Plastics Compos 1987;6(1):36–52.
[20] Rice JR. A path independent integral and the approximate analysis of strain concentration by notches and cracks. J Appl Mech 1968;35:379–86.
[21] Dimarogonas AD. Vibration of cracked structures: a state of the art review. Eng Fracture Mech 1996;55(5):831–57.
[22] Zhang XQ, Han Q, Li F. Analytical approach for detection of multiple cracks in a beam. J Eng Mech 2010;136(3):345–57.
[23] Kageyama K, Kobayashi T, Chou TW. Analytical compliance method for Mode I interlaminar fracture toughness testing of composites. Composites 1987;18(5):393–9.
[24] Swartz SE. Compliance monitoring of crack growth in concrete. J Eng Mech Div 1978;104(4):789–800.
[25] Babuska I, Strouboulis T. The finite element method and its reliability, numerical mathematics and scientific computation. New York: The Clarendon Press, Oxford University Press; 2001.
[26] Fang X. The mechanics of an elastically deforming cantilever beam with an embedded sharp crack subjected to an end transverse load (Doctoral dissertation). Baltimore County: The University of Maryland; 2013.
[27] Habbit SI, Karlsson. ABAQUS documentation. RI, USA: Dassault Systemes; 2013.
[28] Apel T, Sandig AM, Whiteman JR. Graded mesh refinement and error estimates for finite element solutions of elliptic boundary value problems in non-smooth domains. Math Methods Appl, Sci 1996;19:63–85.
[29] Babuska I, Kellogg RB, Pitkaranta J. Direct and inverse error estimates for finite elements with mesh refinements. Numer Math 1979;33:447–71.
[30] Soane AM, Suri M, Rostamian R. The optimal convergence rate of a C1 finite element method for non-smooth domains. J Comput Appl Math 2010;233(10):2711–23.
[31] Parks DM. A stiffness derivative finite element technique for determination of elastic crack tip stress intensity factors. Int J Fracture 1974;10(4):487–502.
[32] Parks DM. The virtual crack extension method for nonlinear materials behavior. Comput Methods Appl Mech Eng 1977;12:353–64.
[33] Anderson TL. Fracture mechanics: fundamentals and applications. CRC Press Inc; 1991. 2nd ed..
[34] Data H, Paris PC, Irwin GR. The stress analysis of cracks handbook. 3rd ed. American Society of Mechanical Engineers Press; 2000.
[35] Liu J, Zhu WD, Charalambides PG, et al. Four-beam model for vibration analysis of a cantilever beam with an embedded horizontal crack. Chin J Mech Eng 2016;29(1):163–79.
[36] Xu YF, Zhu WD, Liu J, et al. Non-model-based damage detection of embedded horizontal cracks. J Sound Vibration 2014;333(23):6273–94.